
Article:
Li, Y. and Qin, N. orcid.org/0000-0002-6437-9027 (2020) Airfoil gust load alleviation by circulation control. Aerospace Science and Technology, 98. 105622. ISSN 1270-9638

https://doi.org/10.1016/j.ast.2019.105622

Airfoil Gust Load Alleviation by Circulation Control

Yonghong Li[1] *and Ning Qin*[2]

Department of Mechanical Engineering, The University of Sheffield, Sheffield, UK.

Abstract

This paper presents a numerical investigation on the gust load alleviation effects based on circulation control (CC) via blowing over airfoil trailing-edge Coanda surface. The NACA0012 airfoil was chosen for the study from subsonic to transonic speeds. The field velocity method is introduced to the unsteady Reynolds averaged Navier-Stokes solutions to simulate responses of the airfoil to arbitrarily shaped gust penetrations. For validation, gust responses to a step change in angle of attack, sharp-edged gusts and one-minus-cosine gusts from the numerical solutions are compared against available theories and other numerical references. Experimental data are used to validate the numerical results of CC. Thereafter circulation control via steady blowing with different momentum coefficients are tested for the gust load alleviation effects in terms of lift coefficients. The results show that circulation control can effectively suppress the lift disturbances caused by the gust for subsonic flows. Most

[1] PhD student
[2] Professor of Aerodynamics, Corresponding author n.qin@sheffield.ac.uk

importantly, CC has a fast frequency response characteristic as more than 50% of the total change in lift coefficient can be obtained within the non-dimensional time $s = U_\infty t/b = 1$. Based on the rapid response characteristic, circulation control via unsteady blowing with dynamically adaptive momentum coefficients proportional to the vertical gust velocities is proposed and tested. The results demonstrate that a near constant lift coefficient can be achieved under gust condition for subsonic incoming flow indicating its potential for real-time adaptive load control. It has been demonstrated that CC is also able to reduce gust load at transonic speed, but it is less effective as compared with that at subsonic speed.

Keywords: circulation control; gust load; airfoil; Coanda effect;

Nomenclature

$\emptyset$ = Wagner function

Ψ = Küssner function

s = non-dimensional time based on semi-chord length

C_L = lift coefficient

w_g = gust velocity

w_0 = peak value of the one-minus-cosine gust velocity

H_g = gust wavelength

C_μ = moment coefficient

$C_{\mu 0}$ = peak value of the momentum coefficient with the one-minus-cosine

profile

$\dot{m}$ = mass flow rate of the CC jet

U_{jet} = jet velocity

Cp = pressure coefficient

b = semi-chord length

c = chord length

U_∞ = freestream velocity

α = angle of attack

M = Mach number

Re_c = Reynolds number based on chord length

1. Introduction

Load control is an important topic in aerodynamics, as it provides an alternative way for drag reduction through decreasing the weight of the aircraft structure. It is well known that the mass of the structure is not determined by the cruise condition but is dictated by the critical load cases such as gust and maneuvering loads. Guo *et al*. [1] indicated that the gust load can be greater than the maneuvering load and produces the most critical load cases in structure design for some aircraft. To ensure aircraft safety, airworthiness authorities have specified typical gust models associated with parameters as requirement for aircraft certification. To cope with these critical load cases, the aircraft structure has to be robust, strong and resilient enough to withstand the forces and stress induced by gusts with a large amount of mass penalty because it is

challenging to design an aircraft structure which is both light and robust. However, from another point of view, if the load on the aircraft can be controlled timely to deal with the gusts, a lighter structure may be designed without compromising safety.

The general principle of gust load alleviation is to use sensors for providing motion feedback signals to some controllers which initiate corresponding deflections of the control surfaces to create the aerodynamic forces and moments needed for attenuating the extra load induced by the gusts. Ailerons, elevators or spoilers are normally used as the control surfaces for gust load alleviation. A common problem in using control surfaces for gust load alleviation is their slow response time. As pointed out by Al-Battal in Ref. [2, 3], control surfaces exhibit low frequency response (≈6Hz), which is ineffective for a typical gust frequency (≈15Hz), due to their large inertia. Little attention has been put on exploring more effective gust load alleviation methods with fast response. Most research activities have been on the design of gust load alleviation systems especially on the design of control laws [4, 5], such as the linear quadratic regulator theory [6], linear quadratic Gaussian method [7, 8], and optimal control algorithms [9].

Fluidic actuators, such as steady blowing or suction, synthetic jets and oscillating jets, have been investigated as means of active aerodynamic flow control methods for many years. But most of these studies focused on altering the momentum balance of the boundary layer to achieve aerodynamic improvement. For example, on top of transition delay and drag reduction, these methods have been proven to be effective to prevent flow separation and augment lift. A wide range of active flow control studies

can be found on the subjects of flow mechanism [10, 11], comparison of effectiveness of different actuators [12, 13], parameter studies including geometry parameters [14], injection or suction parameters [15-17] and excitation parameters [18], influence of locations and layouts [19]. Some significant breakthroughs have been achieved using fluidic actuators for improving aerodynamic performance. Instead of lift augmentation, fluidic actuators can also be used in reducing and managing lift, to find alternative ways for gust load alleviation.

More recently, a few researchers have conducted some initial investigation to explore potential application of fluidic actuators to determine their capability for reducing lift. Based on a NACA0006 airfoil, active flow control using blowing, suction and synthetic jets for gust load alleviation was studied numerically by Xu *et al*. [20]. de Vries *et al*. [21] performed numerical studies at steady conditions for a NACA0018 airfoil at a freestream Mach number 0.176 with a normal jet placed near the trailing edge of the upper surface and a significant reduction of lift was obtained. Al-Battal *et al*. [2] investigated the capability of blowing for lift reduction experimentally. Synthetic jet actuators have been investigated experimentally as load control on the NACA0015 airfoil for altering aeroelastic response such as flutter, limit cycle oscillation and control reversal by Rao *et al*. [22].

Unlike the fluidic actuators mentioned above which mainly work in the direction perpendicular to the airfoil or wing surface, circulation control (CC) by Coanda effect uses the tangential surface jet at the trailing edge to change the aerodynamic properties of the airfoil or the wing. CC using Coanda effect to alter the circulation around the

aircraft wings to generate additional forces for flight control attracted much attention in the recent years. The Coanda effect describes the tendency of a fluidic jet to stay attached to a convex surface as a result of a balance between the low static pressures generated by the jet and the centrifugal force acting on the curving jet. The jet entrains the external flow to follow the jet as to "bend down" over the curved surface which produces a net increase in the circulation of the wing resulting in lift augmentation. Similarly, lift reduction can be achieved if the jet slot is placed on the lower surface. Keller *et al*. [23] conducted a number of experiments to test the effectiveness of CC for lift augmentation or reduction under steady conditions. Numerical work has been done to validate the numerical methods for the simulation of CC by Min *et al*. [24] and Forster *et al*. [25]. The results show that RANS with k-ω SST turbulence model is able to capture the changes of pressure distributions on the airfoil caused by CC. The design and optimization of Coanda surface and the effectiveness of CC as means of maneuverability control of fixed and rotary-wing aircraft have also been studied numerically by Forster *et al*. [25] and Cook et al. [26].

In this paper, the feasibility and effect of gust load alleviation by means of CC will be numerically studied. Unlike most references which confined their studies to low speeds under steady conditions, this study covers a Mach number ranging from 0.3 to 0.8 to gain insights into the effects of CC for unsteady gust load alleviation at both low speed and transonic speed. Firstly, validation work on numerical methods has been done including the simulation of gust load response based on field velocity method and the simulation of CC effects. Based on the validated methods, gust load alleviation effects

based on steady CC jet blowing were carried out under different gust conditions and then unsteady blowing aiming at studying its potential for real-time adaptive load control was performed.

2. Numerical Methods

2.1 RANS Solver

The NASA open-source CFD software CFL3D [27] is used for this work. CFL3D is a structured-grid upwind multi-block CFD code that solves the Reynolds averaged Navier-Stokes equations. A semi-discrete finite-volume approach is used for the spatial discretization, third-order upwind-biased spatial differencing on the convective and pressure terms, and second-order differencing on the viscous terms. An implicit approximate-factorization method is applied for the time advancement for the steady and unsteady flows. The inviscid flux is discretized using Roe's approximate Riemann solver and the viscous flux the second order central difference scheme. MUSCL approach of van Leer is used to determine state-variable interpolations at the cell interfaces. Min-Mod limiter is used in the simulation. Local time-step scaling, multigrid and mesh sequencing are available for convergence acceleration. The solver has a number of turbulence models including 0-equation, 1-equation, and 2-equation models. In this paper k-ω SST model is used for the study.

2.2 Gust Treatment by Field Velocity Method

Using RANS solutions as the tool to calculate aerodynamic responses to step

changes in angle of attack and gusts was first attempted by Parameswaran [28, 29]. The so-called field velocity method or grid velocity method was incorporated into an Euler/Navier-Stokes solver to directly calculate the indicial responses of an airfoil with respect to step changes in angle of attack as well as the penetration of a sharp-edged gust. The field velocity is the velocity of a grid point during the unsteady motion of the airfoil or aircraft, and any change of the motion of the aircraft can be considered as the change of the grid velocity. This method decouples the input parameters. For example, if an airfoil encounters a step change in angle of attack, traditionally it will introduce pitch rate into the result by rotating the airfoil to the target angle of attack. The grid velocity method introduces vertical velocity into the flow domain, which is equivalent to a pure step change in the angle of attack. This characteristic results in a decoupling of the angle of attack time history and the pitch rate time history. This approach also has the advantage to overcome the problems associated with the numerical dissipation of the gust disturbance indicated by Zhou *et al*. [30]. The grid velocity method is a significant advance in gust response research field and has been used to model a wide range of gust interactions. In this paper, the field velocity method is added to the RANS solution code and the present results of gust responses calculated are compared against theories and other numerical references as discussed blow.

3. Validation Problems

3.1 Validation for Gust Response

Any component of gust velocity that is normal to the flight path will change the

effective angle of attack of the aerodynamic surfaces. For a two-dimensional thin flat plate under incompressible and irrotational flow assumptions, two analytical solutions including Wagner and Küssner functions were derived for unsteady lift built-up and were valid for inviscid and incompressible flows. Wagner investigated the lag in the lift generation and formed the Wagner function [31] (Eq. (1)) which provides the indicial built-up of the circulatory part of the lift including the influence of the shed wake due to a step change in the angle of attack. This simple theory has been proved to give accurate indicial responses when the assumptions are valid. The Küssner function [32] (Eq. (2)) describes an analytical formulation for lift responses in the time domain due to a sharp-edged gust based on potential flow theory. These two functions are in terms of the non-dimensional time $s = 2U_\infty t/c = U_\infty t/b$.

$$\emptyset(s) \cong 1 - 0.165e^{-0.0455s} - 0.335e^{-0.3s} \tag{1}$$

$$\Psi(s) \cong 1 - 0.5e^{-0.13s} - 0.5e^{-s} \tag{2}$$

Based on linearized potential equations, Lomax [33] derived exact closed-form expressions of the step responses for short time durations for a thin flat plate in subsonic compressible flow. For a step change in the angle of attack $\Delta\alpha$, the expression is given by

$$\Delta C_L(s) = \frac{4}{M_\infty}\left(1 - \frac{1-M_\infty}{2M_\infty}s\right)\Delta\alpha \tag{3}$$

For a sharp-edged gust with a vertical velocity w_g, the expression of the lift coefficient is given by

$$\Delta C_L(s) = \frac{2s}{\sqrt{M_\infty}} \cdot \frac{w_g}{U_\infty} \tag{4}$$

for both equations (Eq. (3) and Eq. (4)),

$$0 \leq s \leq \frac{2M_\infty}{1+M_\infty} \tag{5}$$

These methods are used to generate aerodynamic response as a function of time to instantaneous changes in aircraft motions. These analytical methods are proven to be accurate in low subsonic speeds and are used as comparable data in literature [20, 28, 29, 34] for CFD validations for gust response. Here, for validation of the gust analysis, gust responses to a step change in angle of attack, a sharp-edged gust and the one-minus-cosine gusts calculated by the present numerical methods are compared to these analytical solutions and other numerical reference results.

3.1.1 Grid Resolution and Numerical Time Step

Grid sensitivity and numerical time step is firstly studied to compare the indicial responses of the lift coefficient for a step change in angle of attack with three different C-type grid resolutions, namely a coarse 121×41 mesh, a medium 221×81 mesh and a fine 421×121 mesh. The finer mesh was generated by refining the grid number in both directions. For these three grid resolutions, the first grid distance from the airfoil is kept constant to make a constant $y^+ \sim O(1)$. The medium grid is shown in Fig. 1.

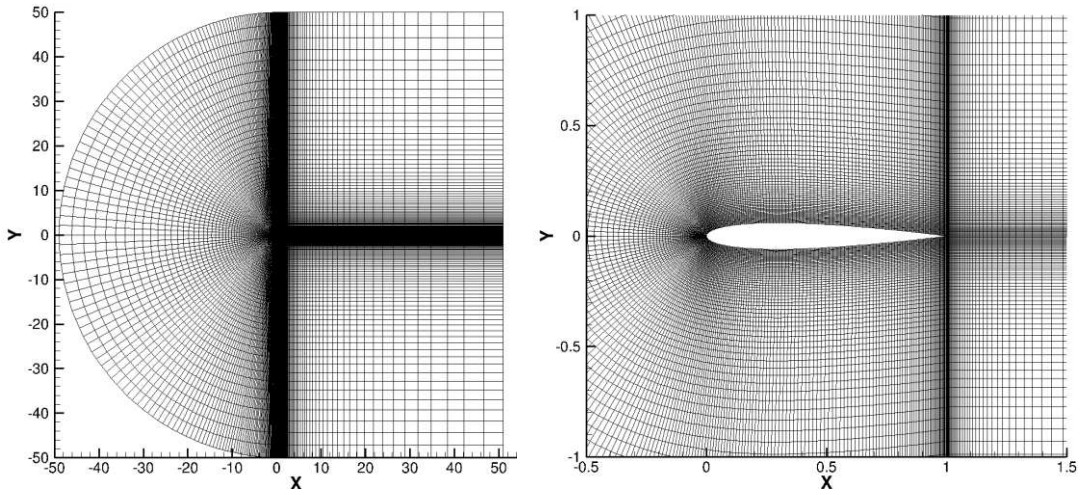

Fig. 1 The medium C-type mesh

The input to the numerical code is the vertical velocity on the computational grid points which is set as

$$w_g = w_0 U_{step}(s) \qquad U_{step}(s) = \begin{cases} 0, s < 0 \\ 1, s \geq 0 \end{cases} \tag{6}$$

Here, $s = U_\infty t/b$ is the non-dimensional time, $U_{step}(s)$ is the step function, $w_0 = 0.08U_\infty$, U_∞ is the freestream velocity. This results in an effective step in angle of attack of approximately 4.6º for M=0.5 from the initial α=0º. The results presented in Fig. 2(a) show that the influence of the mesh resolutions is negligible. The medium grid is chosen for the rest of the validation work.

For the unsteady flow simulations, appropriate time step has to be found in order to obtain an accurate numerical solution and to minimize the CPU time for computations. Three values of time step ($\Delta s = 0.00625, 0.0125, 0.0625$) were used to perform a time step convergence study, see Fig. 2(b). From the results, it can be seen that the lift response of $\Delta s = 0.0125$ is similar with that of $\Delta s = 0.00625$. While, when the time step increases to 0.0625, the lift response deviates from the other two time-step resolutions. Therefore, time step 0.0125 is chosen here.

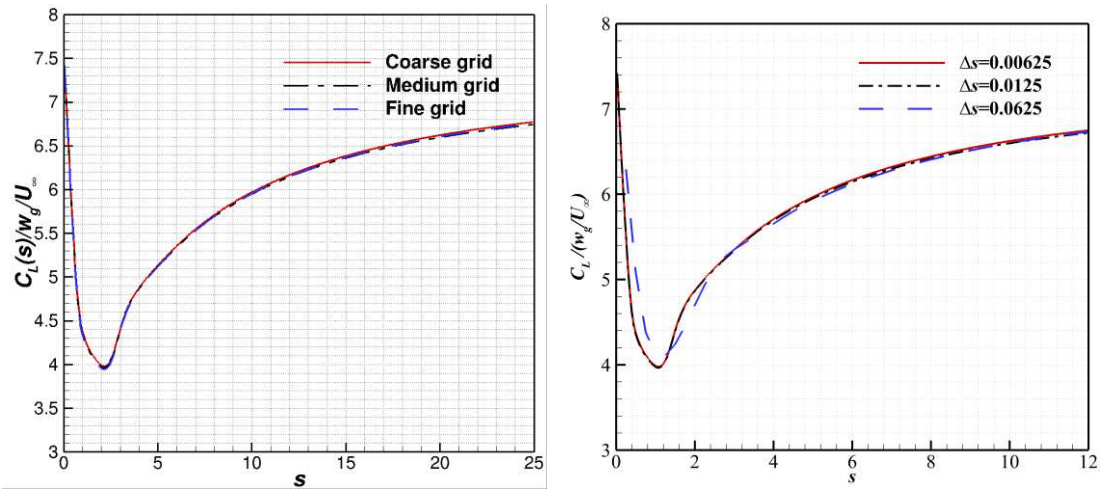

(a) Spatial convergence study (b) Time step convergence study

Fig. 2 Indicial response of lift coefficient for a step change in angle of attack (M=0.5)

3.1.2 A Step Change in Angle of Attack

Three different Mach numbers 0.3, 0.5, 0.8 with a step change in angle of attack, $\Delta\alpha = 4.6°$, are studied. The lift responses are compared with the exact closed-form expressions obtained by Lomax [33] at small time durations, see Fig. 3(a). The present results and the closed-form responses follow each other closely at low Mach numbers. They deviate from each other at higher, compressible Mach numbers. This deviation is due to the fact that the closed-form response was derived based on linearized potential equations for a flat plate at low speeds, and thus does not provide accurate results for finite-thickness airfoils at higher Mach numbers as proposed by Raveh *et al*. [34]. This indicates that the closed-form functions are not valid in transonic ranges, while RANS responses apply throughout this flow range. For Mach numbers 0.3, 0.5 and 0.8, the lift responses for non-dimensional time up to 15 are compared with the data in Ref. [28] and the Wagner function as shown in Fig. 3(b). Good agreement was obtained between

the present results and the numerical reference data which are also based on RANS solutions. The Wagner function is closer to the numerical results for M=0.3 where compressibility is relatively weak. While, large discrepancy appears between the RANS responses and the Wanger function at M=0.5 and 0.8, indicating its limitations to cope with compressibility. Another limitation is that it cannot predict the initial response. Based on Theodorsen's theory [35], the initial part of the unsteady lift is non-circulatory load due to the impulsive motion of the flow which causes the pressure difference on the upper and lower surface of the airfoil. Alternatively, considering the flow is stationary and the airfoil moves impulsively, lift is created by the compression wave on the lower surface and the expansion wave on the upper surface. The non-circulatory lift decays rapidly from its initial value. Unlike the non-circulatory lift, the circulatory lift originates from the vorticity shed into the wake to compensate the change of circulation around the airfoil based on conservation of circulation from Kelvin's theory [29]. The results show that the Wagner function cannot predict the non-circulatory lift. Compared to the closed-form function and Wagner function, the current numerical methods can accurately evaluate the indicial lift response due to the step change in angle of attack from subsonic to transonic speeds.

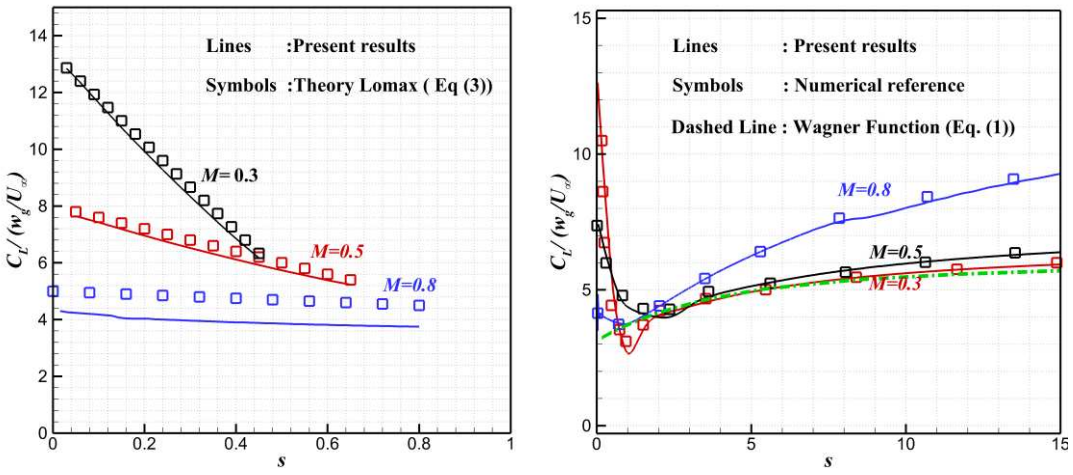

(a) Small time durations (b) Large time durations; numerical reference from Ref. [34]

Fig. 3 Indicial response of lift coefficients for a step change in angle of attack (M=0.3, 0.5, 0.8)

3.1.3 Sharp-edged Gust Response

Firstly, the response to a sharp-edged gust as shown in Fig. 4 with the freestream Mach numbers 0.2 and 0.8 under the gust velocity $w_g/U_\infty = 0.08$ is considered. After the initial time step, the gust travels through the airfoil. In the numerical code, the gust velocity is assigned to all the grid points of the domain where the gust passes.

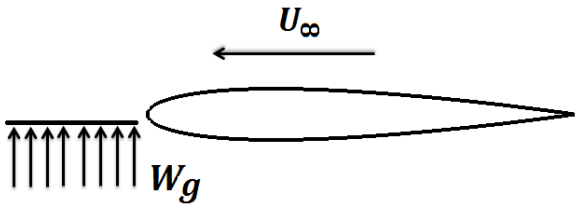

Fig. 4 Sharp-edged gust profile

The Küssner function (Eq. (2)) was used to compare with the present RANS computational results at Mach number 0.2 and 0.8 (see Fig. 5(a)). The present results are normalized by the asymptotic value of the lift coefficient. Overall, a good match between the two methods has been obtained at M=0.2. As was the case of Wagner function for the step change in angle of attack, the Küssner function also show

deviations for high Mach numbers from the RANS results. Mach numbers 0.3, 0.5 and 0.8 are chosen to compare with the Lomax closed-form expression (Eq. (4)) in small time durations as shown in Fig. 5(b). Results are virtually identical at the lower Mach number. While differences become apparent with the increase in Mach numbers, which are similar with the previous study in the indicial responses to a step change in angle of attack.

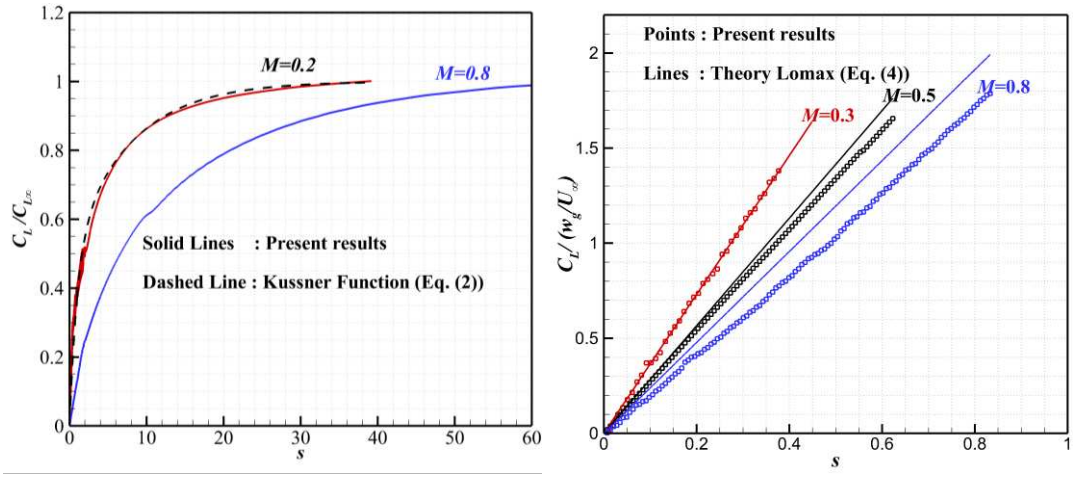

(a) M=0.2, 0.8 (b) M=0.3,0.5,0.8

Fig. 5 Indicial response of lift coefficients to sharp-edged gusts

3.1.4 One-minus-cosine Gust Response

One-minus-cosine gust is a typical discrete gust having the form as

$$w_g = \frac{w_0}{2}\left(1 - cos\left(\frac{2\pi x_g}{H_g}\right)\right) , \qquad \text{for } 0 \le x_g \le H_g \qquad (7)$$

where, w_0 is the magnitude of the peak, or the design gust velocity, x_g is the position of the airfoil in the spatial description of the gust relative to the computation coordinates and H_g is the wavelength of the gust. The gust profile is shown in Fig. 6.

Four cases are simulated and compared with the data presented in Ref. [34]. The first two cases have a freestream Mach number 0.2 with two different wavelengths

$H_g = 5$ and 25 respectively and a constant gust velocity $w_0/U_\infty = 0.017$. The second two cases have a freestream Mach number 0.7 with a constant wavelength $H_g = 5$ and two different gust velocity magnitudes $w_0/U_\infty = 0.017$ and 0.043 respectively corresponding to angle of attacks of 2º and 5º. The comparisons are shown in Fig. 7. The present results and the reference data follow each other closely indicating a good agreement.

The above studies demonstrate that the RANS computational tool, via the introduced field velocity method show good accuracy for gust unsteady responses without the limitation of the analytical functions mentioned above.

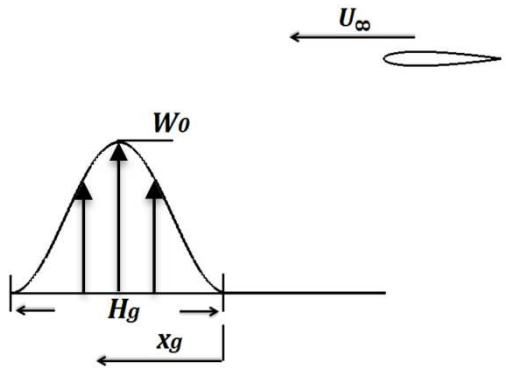

Fig. 6 One-minus-cosine gust profile

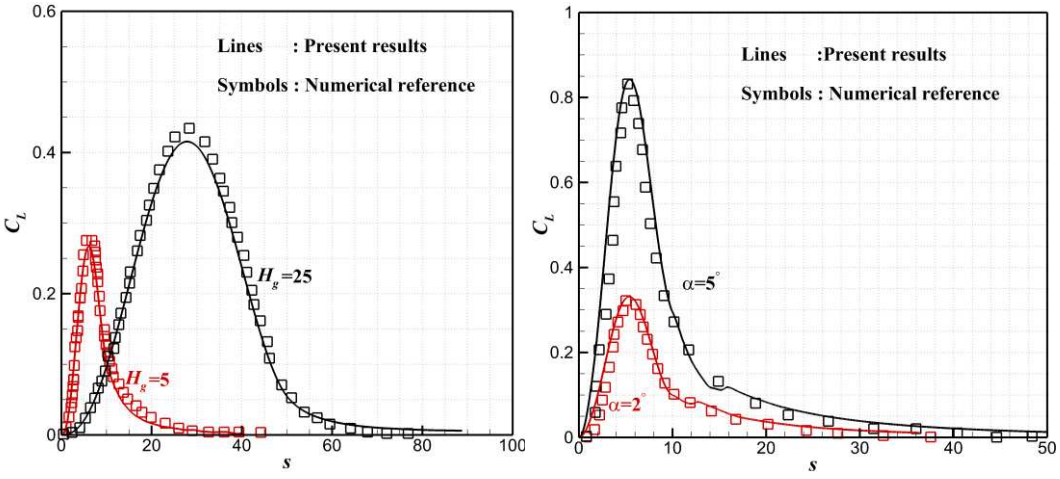

(a) M=0.2 (b) M=0.7

Fig. 7 Comparisions of lift response to one-minus-cosine gusts; numerical reference from Ref. [34]

3.2 Validation of Trailing-edge Circulation Control

Alexander *et al*. [23] conducted a range of experiments to test the effects of CC on a 0.75% cambered elliptical airfoil with a thickness of 6% chord. The span of the wing model is twice chord lengths, with an end plate at one chord length in diameter to minimize the finite span effect. The geometry of the airfoil as well as the 2.98:1 elliptical Coanda surface with a slot height to chord ratio of 0.12% is shown in Fig. 8.

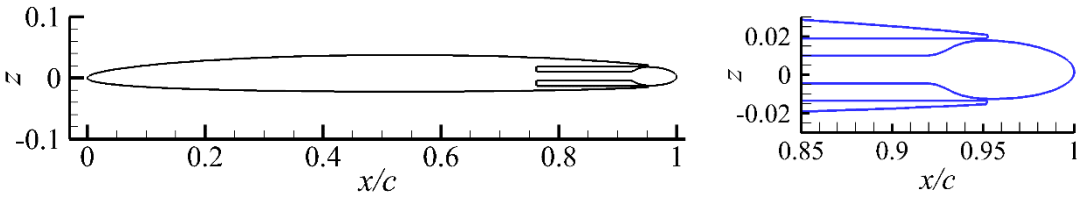

Fig. 8 The elliptical airfoil with Coanda surface

Forster *et al*. [36] investigated the effect of the end plate with a enlarging diameter of 1.1 chord for allowing the structured blocks to wrap around the leading edge of the airfoil while also resolving the flow around the end plate in his CFD validation study. Cruz *et al.* [37] and Forster *et al.* [36] pointed out that modelling of the viscous wall of the splitter plate included in the experiment was necessary for more accurate solutions. Thus, an end plate with 1.1 chord lengths in diameter as well as a circular splitter plate with four chord lengths in diameter are included in the numerical simulation. Fig. 9 shows the generated model and mesh domain used for the simulation.

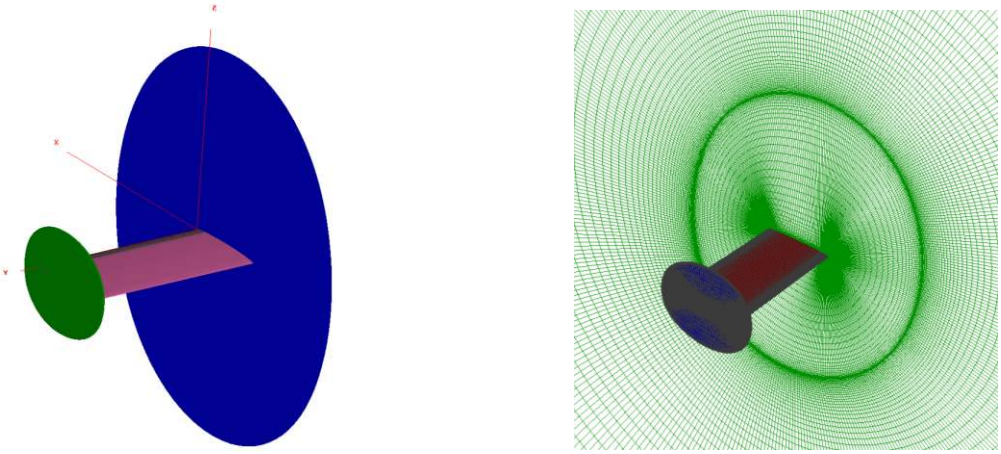

(a) The model with end plat and splitter plate (b) The mesh

Fig. 9 The model and mesh generated based on the experimental model from Ref. [23]

A grid refinement study is performed to investigate the effect of grid density on CC. The medium grid used in the previous study is used here as the baseline airfoil section grid that is 221 cells on the airfoil. 121 cells on the Coanda surface, 149 cells in the wall normal direction and 221 cells over the span of the airfoil are used to create the 3-D mesh. The total grid size is about 11×10^6 and 12×10^6 for the model without and with blowing respectively. Based on this, a coarse mesh with half element of the baseline mesh and a fine mesh with twice of the elements are compared. During the refinement, the distance of the first grid point near the wall was kept constant to keep the $y^+\sim O(1)$.

Fig. 10 shows a comparison of pressure coefficients on the midspan wing section between these three mesh resolutions and the experimental data at M=0.3, α=3º, Re_c=1.0×10^6 for the unblown case. In order to show the 3D effects of the wing model on the pressure coefficients, the computational data of the 2D airfoil is also shown in the figure. The results show large discrepancies in the solutions between the 2D airfoil

and the 3D models. The 2D airfoil case overpredicted the pressure coefficients on both the upper surface and the lower surface, especially near the leading edge. The present results of the pressure coefficients for the 3D model agree well with the experimental data. For the mesh influence, there is negligible difference in the pressure distributions between the medium and fine mesh. The magnitude of the pressure coefficient on the upper surface of the coarse mesh is slightly higher than the other two mesh resolutions, but the pressure coefficients on the lower surface of the three mesh resolutions are in good agreement.

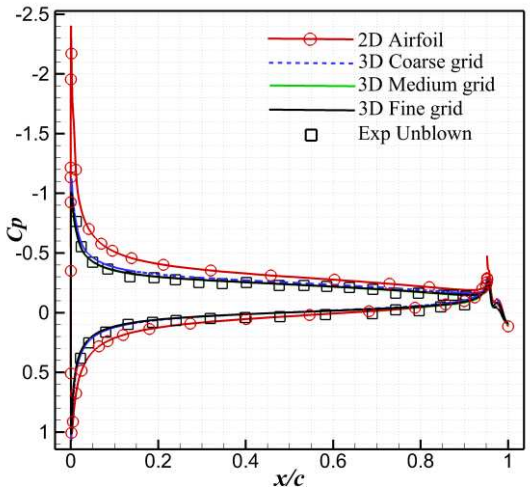

Fig. 10 Comparison of the pressure distributions on the midspan wing section of the unblown case (M=0.3, α=3°)

Fig. 11 shows the comparison of the pressure coefficients on the midspan wing section between the experimental data from Ref. [23] and the present CFD results with the upper slot blowing having a momentum coefficient C_μ≈0.016 and C_μ≈0.054 and with the lower slot blowing having a momentum coefficient C_μ≈0.006 and C_μ≈0.028 at M=0.3, α=3°. Fig. 12 shows the comparison of the pressure coefficients at M=0.8, α=3° for both the upper slot blowing with C_μ≈0.008 and lower slot blowing with C_μ≈0.005 and 0.011.

where, the jet momentum coefficient (C_μ) is defined as

$$C_\mu = \frac{\dot{m}U_{jet}}{q_\infty A} \tag{8}$$

where, $\dot{m}$ is the mass flow rate through the slot exit, q_∞ is the dynamic pressure of the freestream, A is the surface area of the wing and U_{jet} is the jet velocity which can be calculated using Eq. (9) based on the assumption that the jet flow expands out of the slot isentropically to the freestream static pressure.

$$U_{jet} = \sqrt{\frac{2\gamma}{\gamma-1}RT_0\left[1-\left(\frac{p_\infty}{p_{0,plenum}}\right)^{\frac{\gamma-1}{\gamma}}\right]} \tag{9}$$

where, R is the gas constant, T_0 is the total temperature, γ is the ratio of specific heat, $p_{0,plenum}$ is the total pressure in the plenum and p_∞ is the freestream static pressure.

At M=0.3, the computational pressure coefficients on the airfoil surface and the Coanda surface match reasonably well with the experimental data. For the upper slot blowing, the results show that with the increase of momentum coefficient, both the absolute values of the pressure coefficients on the upper and lower surfaces increase resulting in the increment in lift coefficients. The present results also capture the pressure peak at the airfoil leading edge correctly, which experiences an increase in suction pressure with increasing C_μ. The pressures are nearly uniformly shifted over the first 60% of the chord, while the trailing edge and Coanda surface witness larger changes in pressure on both the upper and lower surfaces caused by different momentum coefficients and this behavior is captured well by the present results. For the lower slot blowing, with the increase of momentum coefficients, the absolute

magnitudes of pressure coefficients on both the upper surface and lower surface decrease simultaneously, resulting in a decrease in lift coefficients.

However, for M=0.8, the present numerical methods overpredicted the pressure coefficients on the leading edge upper surface for both the unblown and blowing cases indicating a systemic error between the CFD and the experimental conditions. This might be the wind tunnel wall interference being stronger under transonic speed. However, in general, the present numerical methods captured the pressure coefficients with reasonable accuracy.

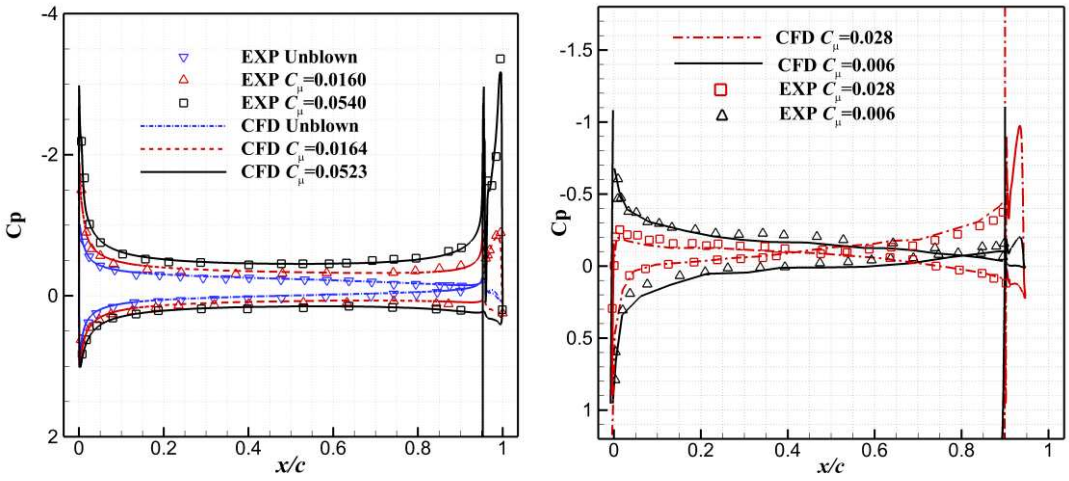

(a) Upper slot blowing (b) Lower slot blowing

Fig. 11 Comparisons of pressure coefficients (M=0.3)

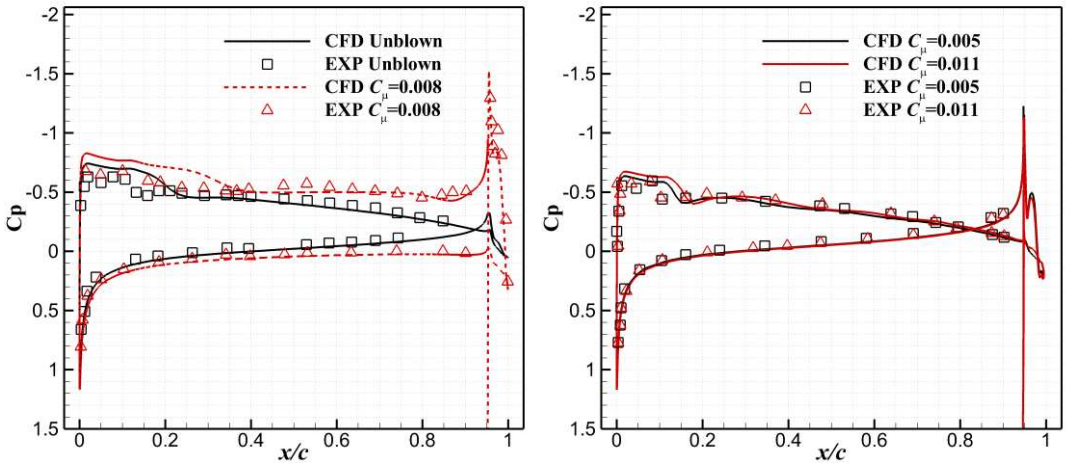

(a) Upper slot blowing (b) Lower slot blowing

Fig. 12 Comparisons of pressure coefficients (M=0.8)

Fig. 13 shows the comparisons of the correlation of the changes in lift coefficients ($\Delta C_L = C_{L_{C_\mu \neq 0}} - C_{L_{C_\mu = 0}}$) due to the variation in momentum coefficients between the experimental data and the present CFD results for both the upper slot blowing and lower slot blowing at M=0.3 and 0.8. According to the studies on CC [26, 38], the effectiveness of CC is not unlimited with the increase of moment coefficient. The 'C_μ-stall' which demonstrates the phenomenon that the increment of lift will experience reduction as the blowing momentum coefficients increase to some extent due to the jet detachment. For both Mach numbers, the present results capture the trends in lift augmentation with increased C_μ. While, in the large C_μ range, the CFD over predicted the value and the reason is unknown. Similar simulation work in Ref. [39] only compared the data of C_μ below 0.04, while we compared the data up to C_μ=0.08. The maximum lift coefficient augmentation is up to about 0.6 for M=0.3. However, for M=0.8, the lift coefficient increment rolls off at a much smaller C_μ compared to that of M=0.3. The maximum lift coefficient augmentation for M=0.8 is only around 0.25 for the upper slot blowing, and 0.13 for the lower slot blowing, indicating the reduced

capability of CC under transonic speed.

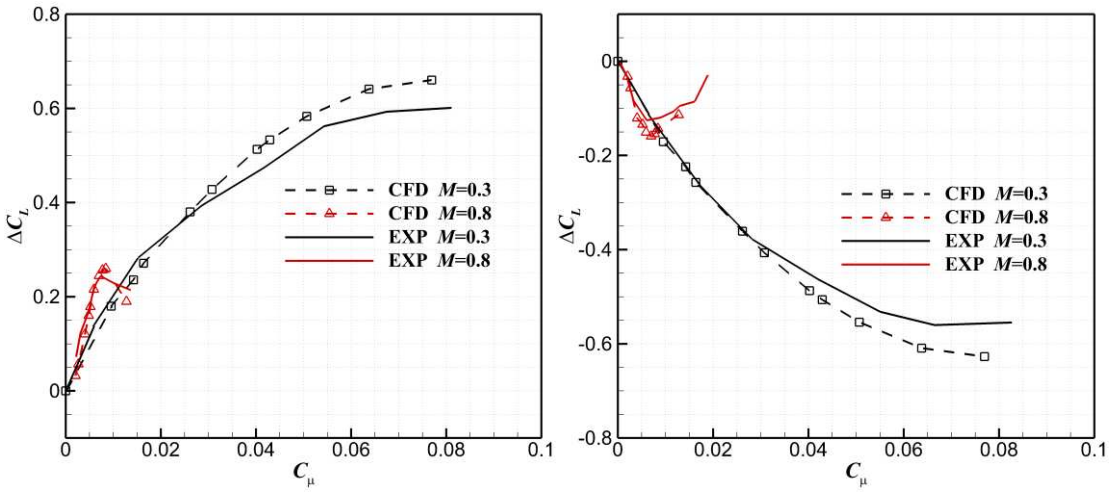

(a) Upper slot blowing (b) Lower slot blowing

Fig. 13 Comparisons of changes in lift coefficients due to C_μ variation under M=0.3 and 0.8, α=3°

Fig. 14 shows the Mach number contours along the midspan wing section for the blowing cases with C_μ=0.005 and 0.015. It is clear to see that when C_μ increased to 0.015, the CC jet detached from the Coanda surface reducing its capacity of entraining the external flow field to follow the jet over the curved surface which is the reason for a net reduction in the circulation of the airfoil. In the meantime, during the calculation for C_μ=0.015, the flow field cannot converge to a steady state, but fluctuates periodically, resulting in the fluctuation in aerodynamic characteristics. Unsteadiness was also observed by Foster *et al*. [36] in the numerical study of transonic CC in the residual of the steady state solution. In general, the CFD tool is proven to be able to provide an accurate representation of the flow through the comparison with the experimental data.

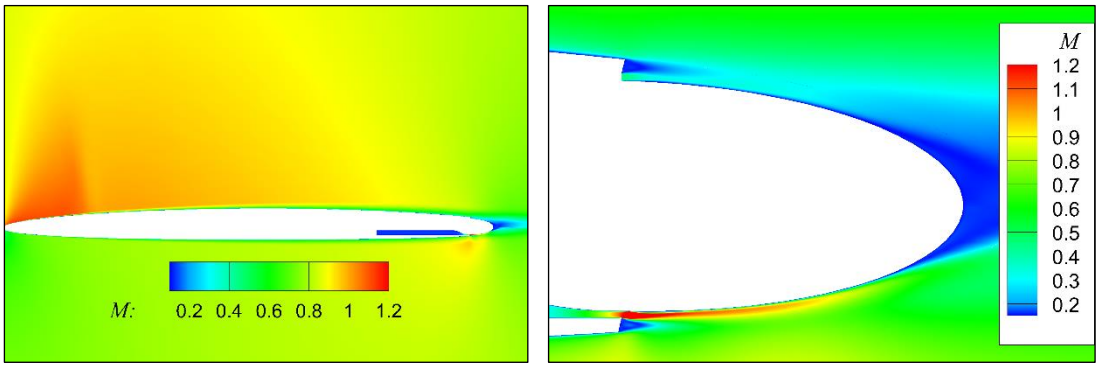

(a) C_μ=0.011

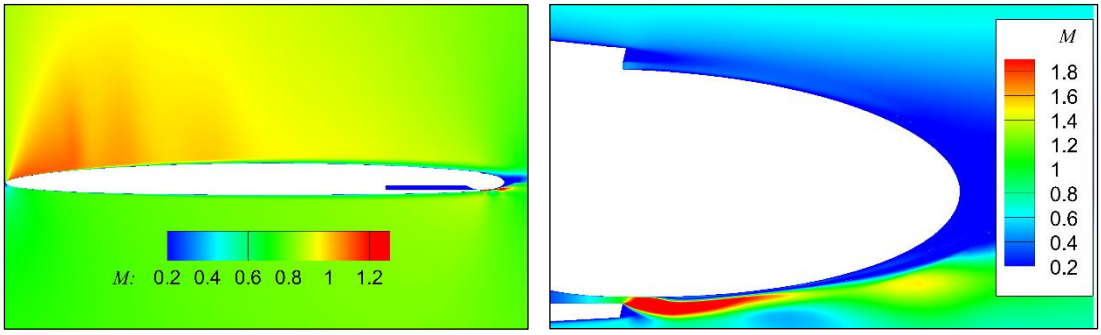

(b) C_μ=0.015

Fig. 14 Mach number contours for M=0.8, α=3°

4. Load Control Effects and Unsteady Actuation of CC on the NACA0012 Airfoil

4.1 Numerical Model Setup of the NACA0012 Airfoil with a Trailing-edge Coanda Surface

The NACA0012 airfoil is used here to investigate gust load alleviation effects by means of CC. In order to include a trailing-edge Coanda surface, the airfoil is truncated at x/c_orig=0.943 (c_orig means the chord length of the airfoil before being truncated) and a semicircular trailing edge with a radius $r/c_{\_orig}$=0.714% is added to the airfoil. Fig. 15 shows the trailing edge of the modified airfoil. According to Wetzel *et al*. [38], the parameters of Coanda surface especially the ratio of the height of the slot exit to the

Coanda surface radius have a substantial influence on the circulation control effect. As this paper does not focus on the parameter study, the ratio of the height of the slot exit to the radius being 1:20 is chosen for this study based on the results by Wetzel et al. [38]. No-slip condition is applied to the Coanda surface and the internal plenum surfaces. A reservoir boundary condition as shown in the red dashed line in Fig. 15 is used to set the desired total pressure and temperature.

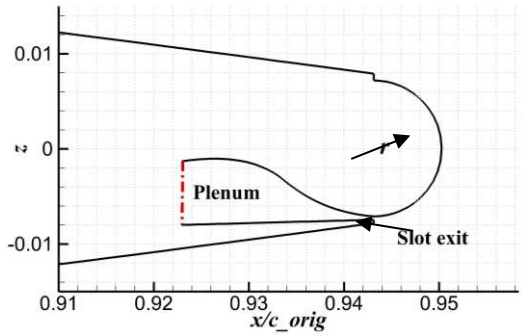

Fig. 15 The trailing edge of the modified NACA0012 airfoil

4.2 Grid Resolution and Numerical Time Step

Based on the grid resolution study on the elliptic airfoil in section 3.2, a grid refinement study is performed on the NACA0012 airfoil with CC. The medium grid used in the previous study is used here as the baseline airfoil section grid that is 221 cells on the airfoil, 121 cells on the Coanda surface and 149 cells in the wall normal direction as shown in Fig. 16. Based on this, a coarse mesh with half element of the baseline mesh and a fine mesh with twice of the elements are compared. During the refinement, the distance of the first grid point away from the wall was kept constant to keep the $y^+ \sim O(1)$. The comparisons of pressure coefficients on the airfoil surface at

M=0.3, α=1º, Re_c=1.0×10^6 and M=0.8, α=1º, Re_c=6.6×10^6 with the blowing momentum coefficients of 0.00142 and 0.0005 respectively, are shown in Fig. 17. The results show that the grid has little influence for subsonic flow but has more influence for transonic flow. This influence is mainly on the shock wave position, as the coarse grid has a closer shock wave position towards the leading edge. Since the pressure distribution of the medium grid matches well with the fine grid, it is used for the following studies.

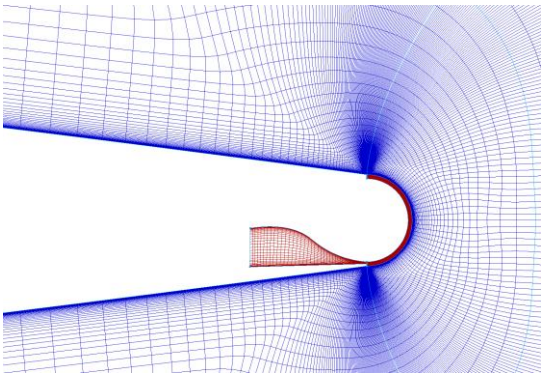

Fig. 16 Mesh around the trailing edge for NACA0012 with Coanda surface

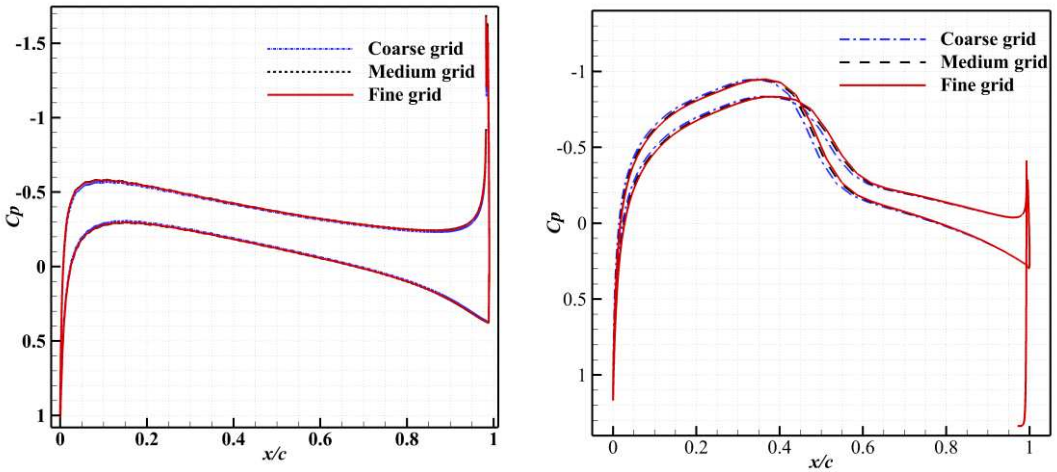

(a) M=0.3 (b) M=0.8

Fig. 17 Influence of the grid resolution under M=0.3 and 0.8, α=1°

To obtain an appropriate time step for the simulation of unsteady CC, a transient actuation of CC is studied under M=0.3 and 0.8, α=1°. Initially, the baseline model is at a convergent steady flow and then the CC jet is activated at s=0 to the maximum

coefficient of 0.0044 and 0.0005 for M=0.3 and 0.8 respectively. Non-dimensional time step Δs from 0.004 to 0.064 is evaluated as shown in Fig. 18. The results show that the lift reaches to the same steady-state final value under different time steps, but the time step influences the initial lift responses after the CC jet is activated. This influence becomes negligible between Δs=0.004 and 0.016 for both Mach numbers. Δs=0.004 is chosen for the following studies. Also shown in the results is that the flow reaches to a steady state between s=5 and 8 after the activation of CC jet for both cases.

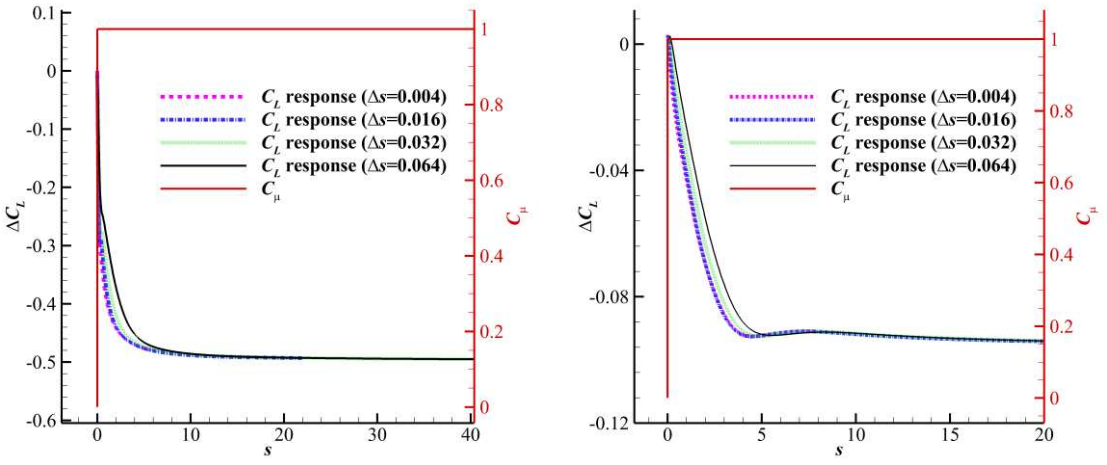

(a) M=0.3 (b) M=0.8

Fig. 18 Influence of the time step under M=0.3 and 0.8, α=3°

4.3 Load Control Effects of CC under Steady Conditions

To get a quantitative understanding of the load control capability of CC on the NACA0012 airfoil, the load control effects in terms of lift coefficient reduction are examined under a series of momentum coefficients. The freestream condition is M=0.3 and 0.8 at α=3°. The lift coefficient reduction under a range of blowing momentum coefficients is shown in Fig. 19. The load control effects are similar to the elliptic CC airfoil in the previous validation study that CC has a much stronger load control

capability under subsonic incoming flow than the transonic one. It is noticeable that the maximum reduction in lift coefficient reaches to 1.34 at M=0.3, α=3º. While, this value is only 0.15 when the freestream condition is M=0.8, α=3º. As the lift coefficient will start to oscillate when the blowing momentum coefficient increases to a certain value, the standard deviation is also shown for the case with oscillation in the figure. For M=0.8, the lift starts to oscillate when the momentum coefficient is above 0.001. The 'C_μ-stall' point is around C_μ=0.0013 and 0.0095 for M=0.3 and 0.8 respectively.

Fig. 20 shows the effect of varying the angle of attack on the lift characteristics of CC using C_μ=0.0035 and 0.0004 for M=0.3 and 0.8 respectively. For M=0.3, a near constant lift reduction of ΔC_L=-0.36 is obtained, while a decreasing load control effect is observed for M=0.8 with the increasing angle of attack.

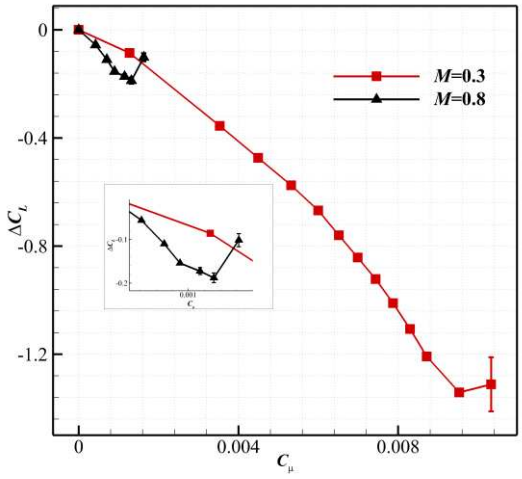

Fig. 19 Lift coefficient reduction under a range of momentum coefficient at steady conditions (M_∞=0.3 and 0.8, α=3º)

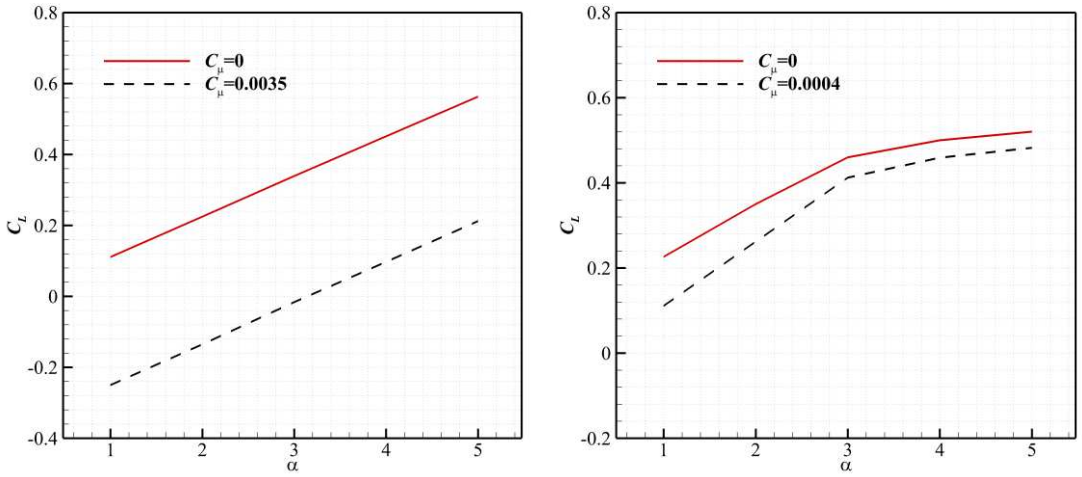

(a) *M*=0.3 (b) *M*=0.8

Fig. 20 Effect of angle of attack on load control at *M*=0.3 and 0.8

4.4 Unsteady Actuation of CC

For high-frequency gust alleviation, the unsteady response of lift is the key factor. To understand the behavior of the response of lift under unsteady actuation of CC, the periodic actuation of CC with the following expression in Eq. (10) is studied under *M*=0.3 and 0.8, α=1°.

$$C_\mu = C_{\mu 0}\sin(2\pi f \cdot s) \tag{10}$$

The reduced frequency k= $\pi f c/U_\infty$. For a typical gust length which is 12.5c defined by EASA CS-25 [40], the reduced frequency is about 0.25. Three values of reduced frequency of 0.125, 0.25, 0.5 are used to compare the effects of actuation frequency. The maximum momentum coefficient $C_{\mu 0}$ is 0.0044 and 0.0005 respectively, for *M*=0.3 and *M*=0.8. The results reflected in the hysteresis loops of the lift changes as a function of the blowing momentum coefficients are shown in Fig. 21. All loops are clockwise. It is clear that the hysteresis loops all start and end with negative slopes indicating effective load control ability with the increasing blowing

momentum coefficients. While, with the increasing reduced frequency, the load control effects decrease for both Mach numbers as the slope decreases, and the phase lag increases. This effect is more apparent under M=0.8 as indicated in Fig. 21 (b), as the slop is quite small even though it is still negative when k=0.5 indicting a limitation for high-frequency actuation of CC under transonic incoming flow. This limitation is substantially related to the inherent weak of CC entrainment under transonic flow demonstrated previously.

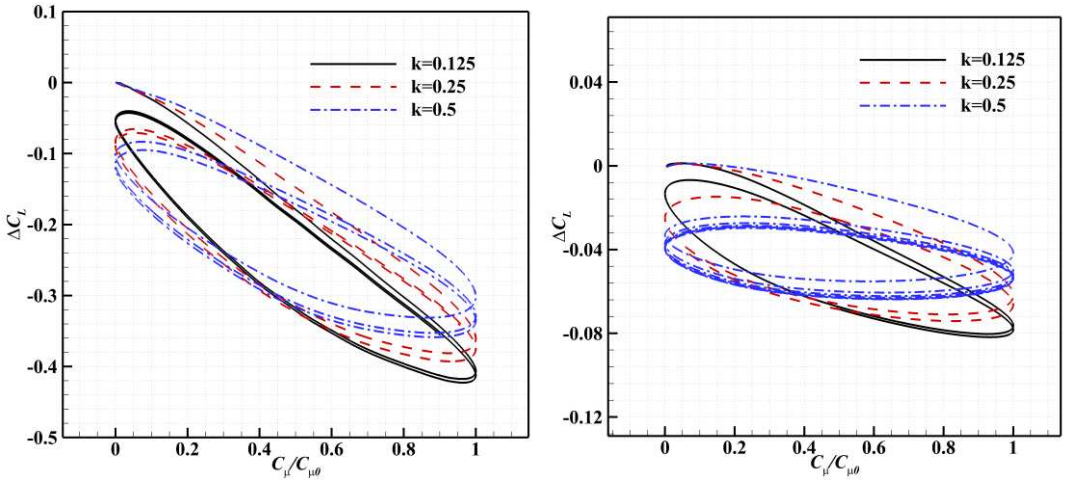

(a) M=0.3 (a) M=0.8

Fig. 21 Lift response with unsteady actuation of CC

5. Gust Load Alleviation by CC

5.1 Case Study at M=0.3

5.1.1 Gust Load Alleviation Effects of CC under a Step Change in Angle of Attack

Initially, gust load alleviation effects are tested to a step change in angle of attack $\Delta\alpha = 4.6°$ with a cruise state of M=0.3, α=1°, Re_c =1.0×10^6. Three different

momentum coefficients which are switched on instantaneously at s=0 are applied to the test and the gust alleviation characteristics are compared to the gust response of the baseline model without CC as shown in Fig. 22. As can be seen from the results that CC has significant effects on gust load alleviation. With the increase of momentum coefficients, the gust load is better controlled. To be specific, the amplitudes of the lift coefficients are reduced about 25%, 54% and 78% compared to the baseline model after s=10 with C_μ=0.0015, 0.0028 and 0.004 respectively. Interestingly, with C_μ= 0.004, the lift coefficient is in the similar value with that of the steady state after s=2 when the non-circulatory lift decay. That is to say with a certain value of moment coefficient, CC can completely control the gust load. Fig. 23 shows the time history of the lift coefficient reduction relative to the baseline model. The numbers in percentage in Fig. 23 mean the ratio of lift coefficient reduction at the current non-dimensional time s to that of the total lift coefficient reduction at $s\rightarrow\infty$, that is $\frac{(\Delta C_L)_s}{(\Delta C_L)_{s\rightarrow\infty}}$. From the result we can see that more than 50% of the total change in lift coefficient can be obtained within the non-dimensional time $s = U_\infty t/b$=1. This result is consistent with the findings by de Vries *et al*. [21] who conducted experiments and simulations using microjets for active aerodynamic load control on the NACA0018 airfoil at M=0.176. As the freestream speed is U_∞=102 m/s, then the non-dimensional time s =1 refers to the real time t=0.0098 second and frequency f=102 Hz. Compared to current gust load alleviation techniques comprise of ailerons and spoilers which exhibit a response frequency of approximately 6 Hz proposed by Al-Battal *et al*. [3], gust load alleviation by means of CC has a faster frequency response characteristic.

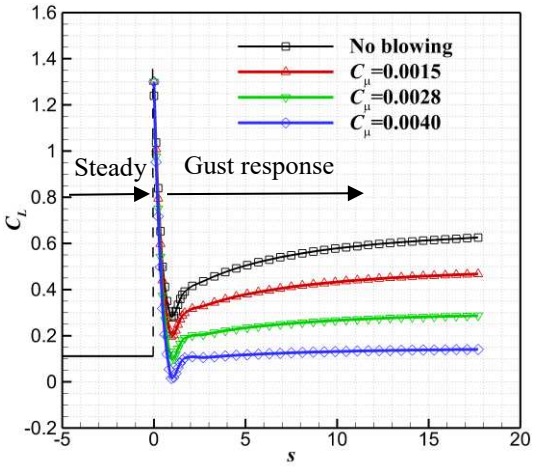

Fig. 22 Gust alleviation characteristic to a step change in angle of attack

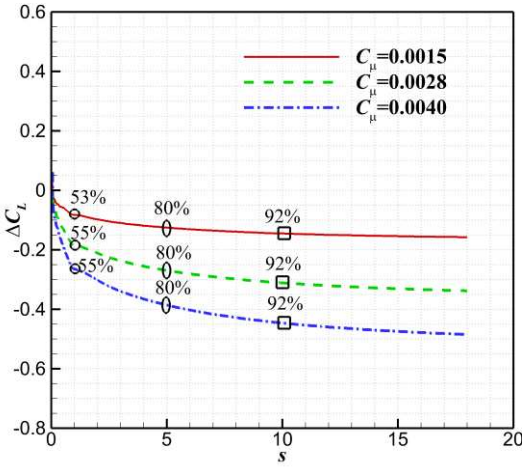

Fig. 23 Relative lift coefficient reduction to the baseline model

The streamlines of the baseline model and the model with C_μ=0.004 at s =5 are shown in Fig. 24 and Fig. 25. A significant difference of the streamlines exists in the rear region of the airfoil of the two models. The streamlines from the upper surface and lower surface of the baseline model are almost symmetric about the airfoil centerline at the rear region. However, due to the high-speed jet from the slot exit, streamlines are entrained upwards obviously at the rear area of the model with CC, resulting in the streamlines from the upper surface being deflected upwards by the entrained flow from lower surface. With the increase in jet momentum coefficient, the streamlines around the lower trailing-edge surface is entrained more upwards as shown in Fig. 26. This effect causes an increase in flow velocity near the lower surface, but a reduction near the upper surface. This difference in flow velocity near the airfoil surface makes a significant change in pressure coefficients on the airfoil as shown in Fig. 27. In general, with the increase in momentum coefficients, the pressure coefficients on the upper surface increase and decrease on the lower surface, resulting in a total lift reduction.

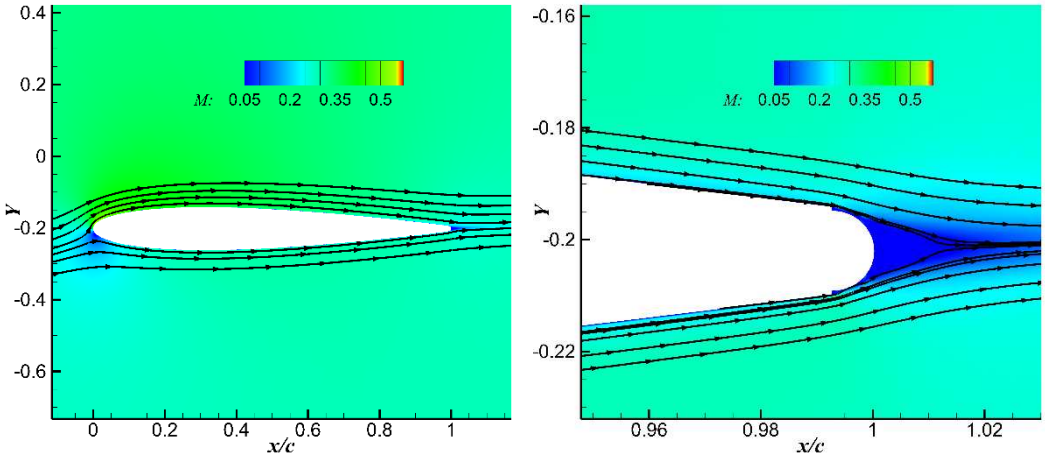

Fig. 24 Streamlines of the baseline model at s =5

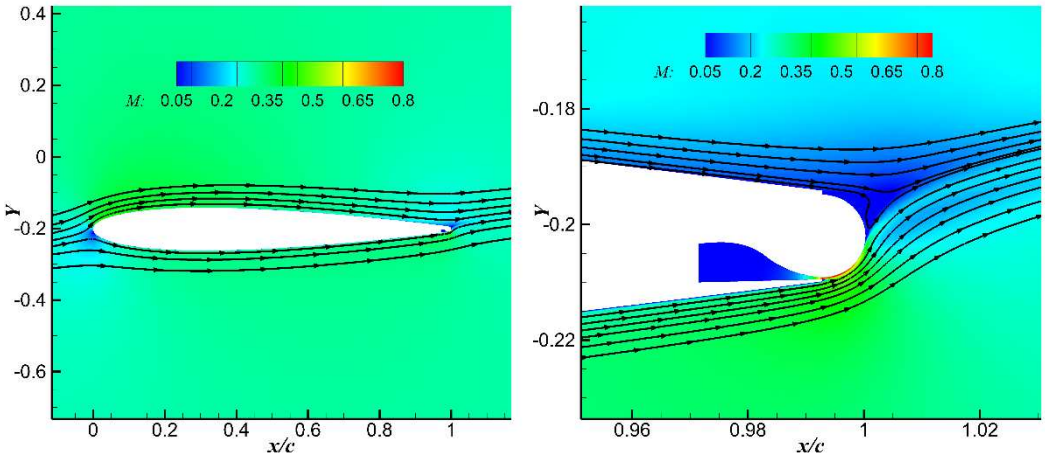

Fig. 25 Streamlines of the model with C_μ=0.004 at s =5

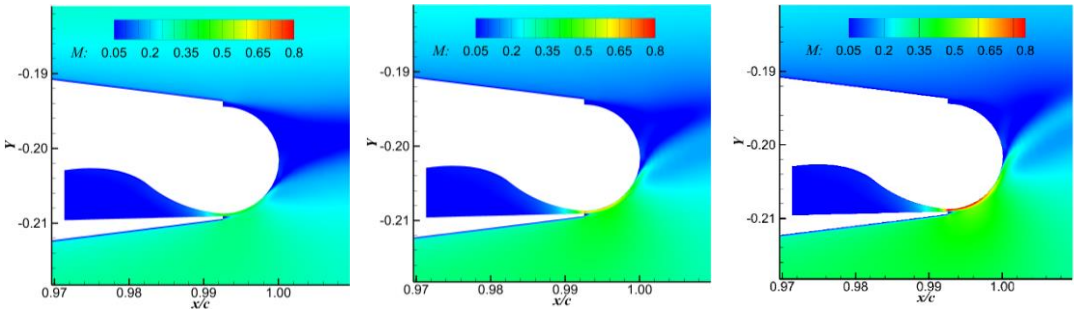

(a) C_μ= 0.0015 (b) C_μ= 0.0028 (c) C_μ= 0.004

Fig. 26 The entrainment characteristic with the increase in momentum coefficient

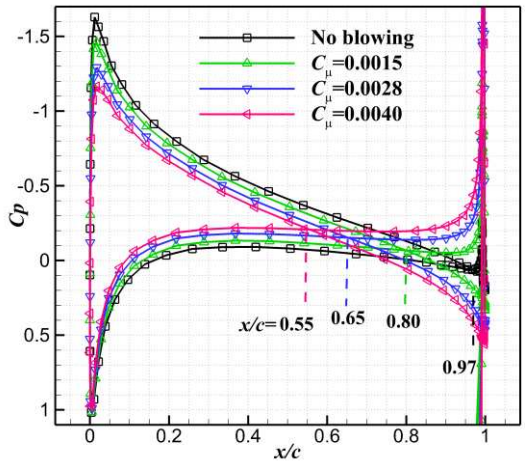

Fig. 27 Comparison of pressure coefficients due to the change in momentum coefficients (s=5)

5.1.2 Gust Load Alleviation Effects of CC under One-minus-cosine Gusts

Gust load alleviation effects are analyzed with the one-minus-cosine gust with the velocity $w_0/U_\infty = 0.033$ and the wavelength of the gust is about 6c corresponding to s=12. The gust profile in non-dimensional time domain can be expressed in Eq. (11) and is shown in Fig. 28. At s=0, the gust hits the leading edge of the airfoil and travels past the airfoil with the freestream Mach number 0.3. The angle of attack of the airfoil is kept to α=1°.

$$\begin{cases} w_g = 0 & (s < 0) \\ w_g = \frac{1}{2} w_0 \left(1 - cos\frac{2\pi s}{12}\right) & (0 \le s \le 1 \\ w_g = 0 & (s > 12) \end{cases} \tag{11}$$

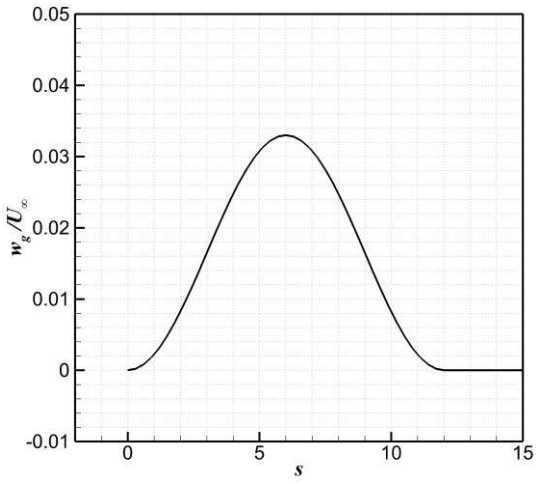

Fig. 28 The one-minus-cosine gust profile

a. CC with Constant Blowing Moment Coefficient

Firstly, the control strategy with the CC jet on at s=0 and jet off at s=12 with a constant moment coefficient C_μ=0.0028 is applied to the test. The gust response is compared to that of the baseline model without CC jet blowing as shown in Fig. 29. The CC jet is turned on at s=0 (point a), from when the lift coefficient saw a sharp decrease to point b (s≈1) due to the rapid response characteristic mentioned above. From Fig. 30 which shows the alleviation magnitude of the lift coefficient, similar gust load alleviation characteristic to the previous result in Fig. 23 can be observed. That is more than 50% of the total change in lift coefficient can be obtained within the non-dimensional time s=1. After the jet is turned off at point c, the lift coefficient increases sharply and generally returns to the value in the steady state. Compared to the baseline model, the CC model does reduce the peak gust load significantly. However, the magnitude of the lift coefficient still has a large fluctuation under the gust perturbation

indicating that it is improper to use a constant blowing momentum coefficient for a discrete gust perturbation. A straightforward idea is to use an unsteady blowing with the jet momentum coefficient changing proportionally to the variation of the gust velocity.

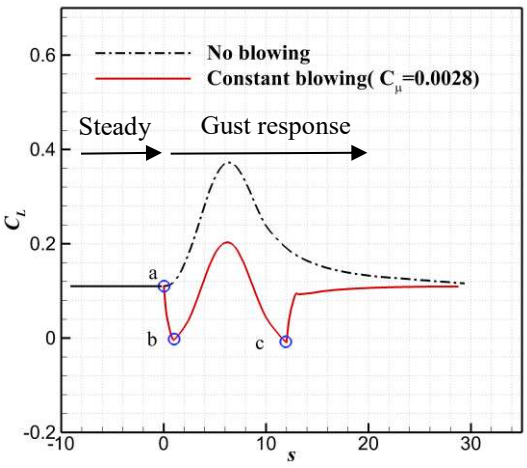

Fig. 29 Gust alleviation characteristic to one-minus-cosine gust with constant blowing

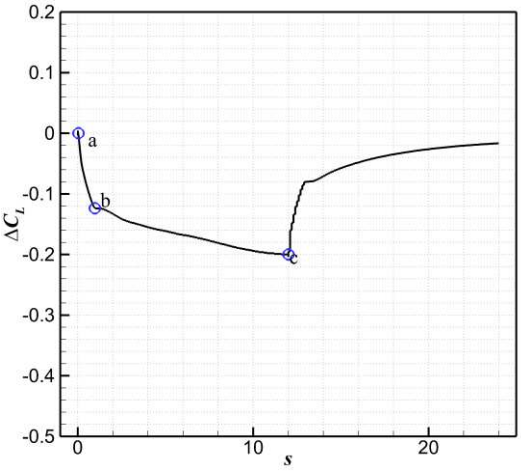

Fig. 30 Relative lift coefficient reduction to the baseline model

b. CC with Unsteady Blowing Moment Coefficient

For the understanding of the time response of the unsteady blowing, the momentum coefficient with a 'one-minus-cosine' profile as same as that of the gust is employed which can be expressed as

$$\begin{cases} C_\mu = 0 & s < 0 \\ C_\mu = \frac{1}{2} C_{\mu 0} \left(1 - cos \frac{2\pi s}{12}\right) & 0 \le s \le \\ C_\mu = 0 & s > 12 \end{cases} \tag{12}$$

where, $C_{\mu 0}$ is the magnitude of the peak momentum coefficient. Two different cases with the peak momentum coefficients of $C_{\mu 0}$ =0.0028 and 0.004 are applied. The freestream condition is the same as the former case study. The time responses of lift

coefficients without gust penetration are firstly evaluated in order to view the time responses of the unsteady blowing under steady freestream conditions. The response of lift coefficients together with the profiles of the momentum coefficients are shown in Fig. 31. From the results, it can be seen that the designed momentum coefficients with both peak values are symmetric about the peak values at s=6 as indicated by the solid red line marked **b**. For example, the momentum coefficient at point **a** (s=4) is the same with the value at point **c** (s=8). While, from the curves of the lift coefficient response, it is clear that the response is not symmetric about s=6 as the momentum coefficients do. Meanwhile, the value of the reduction in lift coefficient does not peak at s=6 where the momentum coefficient has the largest value, but peaks at afterwards about s=7 (point **d**). It is easy to understand that even though CC jet has a rapid response characteristic, it still needs time to react and develop, and the deployed momentum coefficient will have an influence on the subsequent flow field resulting in 'time lag' in the response of lift coefficient. However, the 'time-lag' is small as indicated from Fig. 31, which is also benefit from its fast response characteristic.

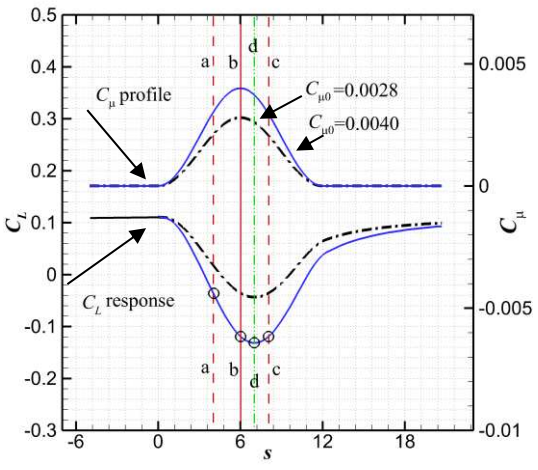

Fig. 31 The profiles of the unsteady momentum coefficients and the corresponding response of lift

coefficients under steady conditions

The gust load alleviation effects of these two unsteady CC jets are then studied under the gust penetration with the velocity expressed in Eq. (11). The gust response in terms of lift coefficients is shown in Fig. 32 together with the response of the baseline model without blowing. As shown in the result, compared to the baseline model, these two unsteady jets reduce the peak lift coefficients caused by gust penetration by approximately 54% and 85% respectively. For the characteristic of the 'time-lag' in response, the high deployed momentum coefficients around and after s=6 (see the momentum coefficient profile in Fig. 31) will influence the lift response afterwards making the lift coefficients even lower than the steady state at non-dimensional time between s=8 and s=11 (where the gust velocity diminishes generally) for the jet with $C_{\mu 0}$ =0.0040. However, compared to the steady blowing case shown in Fig. 29, the fluctuation of the lift coefficients using unsteady blowing is much smaller under the same gust perturbation, indicating a better control effect. While, a further question may be asked about whether CC has the capability to control the gust load timely with adaptive characteristics?

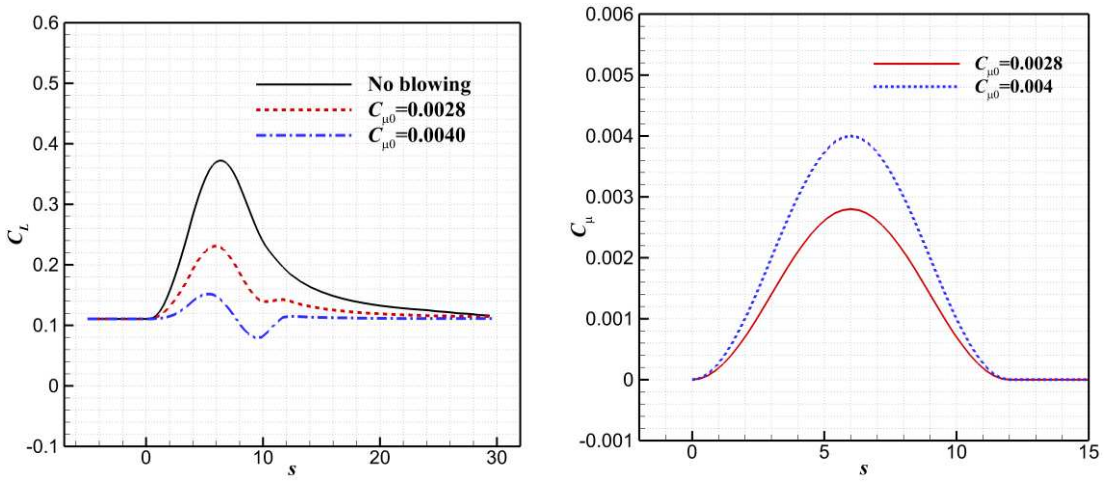

(a) Lift response (b) C_μ profile

Fig. 32 The response of lift coefficients with unsteady CC jet blowing under gust condition

c. CC with Designed Adaptive Blowing Moment Coefficient

From the results of the unsteady CC jet studied previously, even though the profile of the gust load alleviation value in terms of lift coefficients is not completely the same as that of the deployed momentum coefficients in the time domain, the gust load alleviation value is indeed proportional to the momentum coefficient with a small 'time-lag' effect. For this reason, CC jet is proposed to have the capability to control the gust load timely with adaptive characteristics. To test this, based on the data for $C_{\mu 0}$ =0.0028 or $C_{\mu 0}$ =0.0040 shown in Fig. 32, the relationship of the lift coefficient reduction caused by CC jet named $\Delta C_L(CC)$ and s relative to $C_\mu(s)$ can be interpolated, which can be expressed as

$$C_\mu(s) = f_1(s, \Delta C_L(CC)) \tag{13}$$

where, f_1 is the fitting function based on the data of $\Delta C_L(CC)$, s and $C_\mu(s)$. A quadratic polynomial function is chosen here. Based on this function, from the gust response value of the baseline model, the increment of the lift coefficient due to the

gust, named as $\Delta C_L(gust)$ can be obtained. Therefore, to compensate $\Delta C_L(gust)$ with the control of unsteady CC jet, the required value of the momentum coefficient can be predicted by the expression of Eq. (13) as

$$C_\mu(s) = f_1(s, -\Delta C_L(gust)) \tag{14}$$

The profile of the predicted momentum coefficients marked as 'Adaptive' is shown in Fig. 33. For the comparison, the momentum coefficients with the same peak value but has a 'one-minus-cosine' profile are also shown in the figure. As expected, the values of the momentum coefficients after *s*=6 decrease and the point of the peak value shifts forwards a little due to the small 'time-lag'.

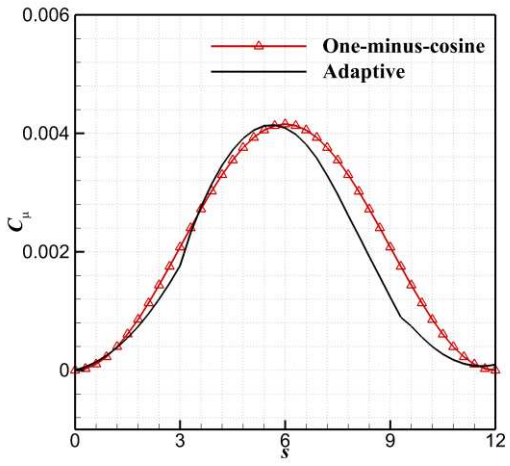

Fig. 33 The profile of the predicted momentum coefficient

The predicted momentum coefficients are applied in the following test case and the results are shown in Fig. 34 marked as 'Adaptive blowing'. From the results, it is clear that dynamically adapting the momentum coefficient effectively counteracts the gust load and a near constant lift coefficient is obtained under gust perturbations. It is true that the adaptive blowing of this study is obtained under a certain gust perturbation

and freestream condition. The function obtained in Eq. (13) is not appropriate for all gust perturbations. In practice, a database of the ability of CC for various momentum coefficients according to different gust velocities and freestream conditions should be set for an open-loop or closed-loop control. This case study indicates the capability of CC for adaptive gust load control under low subsonic speed due to the strong ability of CC for lift reduction, the fast response characteristic and the small 'time-lag' in response.

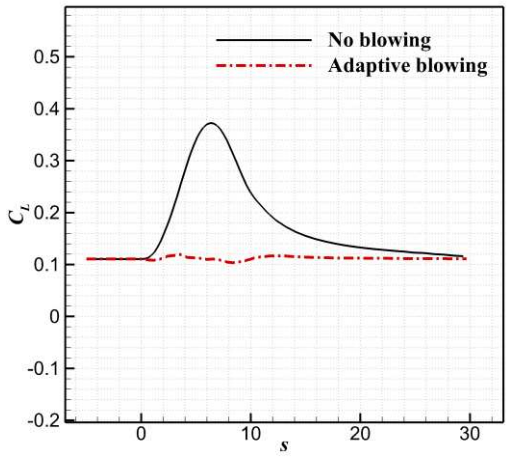

Fig. 34 The gust response of the adaptive blowing

5.2 Case Study at *M*=0.5

At *M*=0.5, gust load alleviation effects are analyzed under two blowing conditions. One is the unsteady blowing with the one-minus-cosine profile, where the peak momentum coefficient is $C_{\mu 0}$ =0.0024. The response of this unsteady blowing is used to design an adaptive blowing through the same method described previously for the test of adaptive control under *M*=0.5. The gust is the one-minus-cosine gust with the velocity $w_0/U_\infty = 0.033$ and the wavelength of the gust is about $10c$ corresponding

to s=20. The freestream condition is M=0.5, α=1°, Re_c =1.67×10^6.

The gust responses in terms of lift coefficient under these two blowing conditions and the condition without blowing are shown in Fig. 35. Similar to the results in the case study at M=0.3, the unsteady blowing is able to alleviate the gust load dramatically and a near constant lift coefficient is also obtained under the designed adaptive blowing, which means the gust load in this study condition can also be completely suppressed.

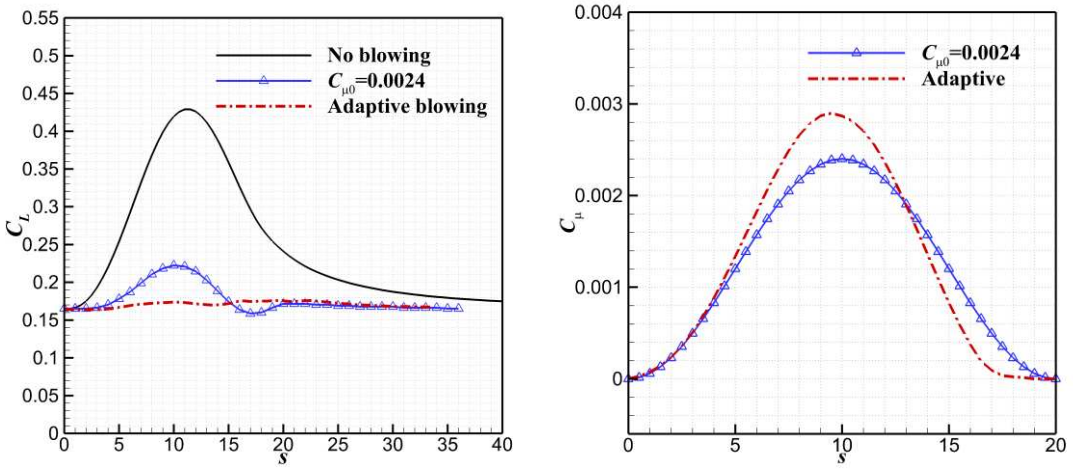

(a) Lift response (b) C_μ profile

Fig. 35 The gust response at M=0.5

5.3 Case Study at M=0.8

To test CC for gust alleviation at transonic speeds, the one-minus-cosine gust with gust velocity w_0/U_∞=0.033 and wavelength of 24c corresponding to s=60 is applied for the flow conditions of M=0.8, α=1°, Re_c=6.6×10^6. The momentum coefficients of the unsteady blowing with one-minus-cosine profile having two peak values $C_{\mu 0}$=0.001 and $C_{\mu 0}$=0.0014 respectively are employed. The results are shown in Fig. 36. For both blowing cases, the gust loads are alleviated through the whole gust working duration

and the peak gust load is reduced by about 48% for the blowing case with $C_{\mu 0}$=0.001. However, when the maximum blowing momentum coefficient increases 0.0014, the peak value of the lift coefficient does not decrease but increase coupled with slight fluctuations at s=17 with C_μ=0.00091, which indicates the occurrence of 'C_μ-stall'. As shown in Fig. 36(b), the lift starts to oscillate at the first marked red point (s=17, C_μ=0.00091) and ends at the second one (s=40, C_μ=0.001). These values are close to the C_μ value where the lift starts to oscillate under the steady free-stream condition shown in Fig. 19 at M=0.8. But for the $C_{\mu 0}$=0.001 case, the lift response does not start to oscillate at the C_μ value as $C_{\mu 0}$=0.0014 case does. The reason for this is so far unknown. Fig. 21 has demonstrated the influence of the reduced frequency of CC jet actuation as with the increase in the rate of change of C_μ, the load control effect decreases. For the detachment above the 'C_μ-stall', the dynamic response characteristics of 'C_μ-stall' under dynamic actuations is worth to be studied by higher order turbulence modeling. The Mach number contours around the trailing edge of the airfoil at the non-dimensional time s=30 under these two blowing conditions are shown in Fig. 37. It illustrates that the entrainment ability of the Coanda jet becomes weaker for $C_{\mu 0}$=0.0014 as the jet flow leaves apparently more forward from the Coanda surface compared to the blowing case with $C_{\mu 0}$=0.001. Compared to the case studies under subsonic speeds, the effect of CC for gust load alleviation declines due to the 'C_μ-stall' occurs at a much smaller momentum coefficient. This effect may be alleviated due to the fact that the gust velocity tends to be smaller at transonic range than that at subsonic range since the aircraft fly at a much higher altitude with the increase in cruise speed.

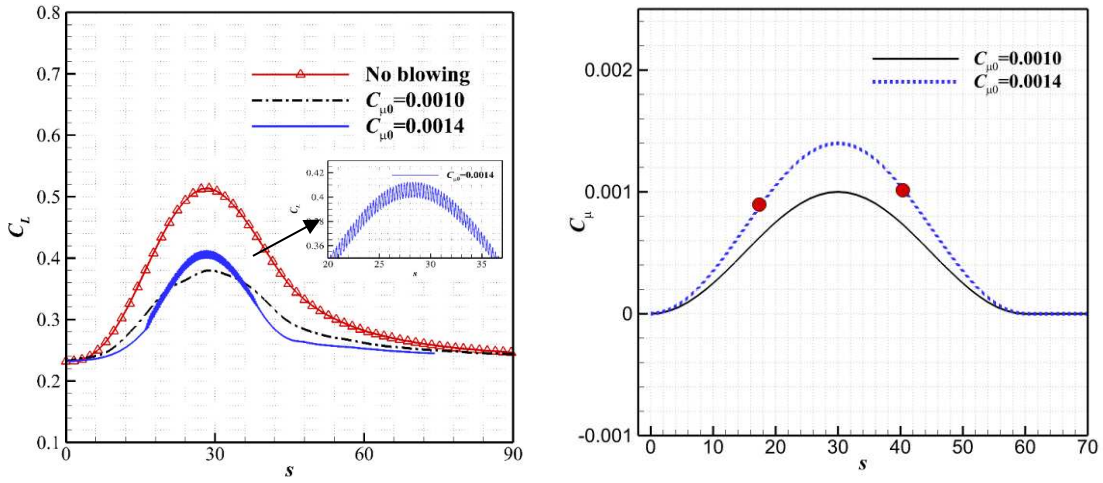

(a) Lift response (b) C_μ profile

Fig. 36 The gust response at M=0.8

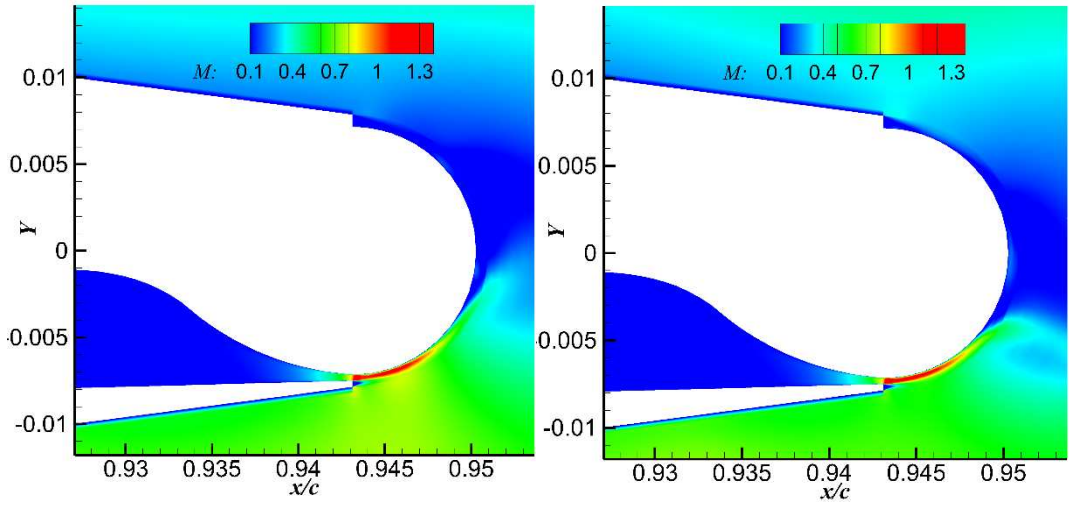

(a) $C_{\mu 0}$=0.0010 (b) $C_{\mu 0}$=0.0014

Fig. 37 The Mach number counters around the rear region of the airfoil at s=30

6. Conclusions

Gust load alleviation effects based on circulation control via blowing over trailing-edge Coanda surface on an airfoil at M=0.3, 0.5 and 0.8 are numerically investigated. Firstly, comparisons of the CFD solver against the available data are carried out for validation of gust responses and CC. Circulation control via steady blowing and

unsteady blowing are tested under different gust conditions, and some findings are summarized below

Circulation control via blowing over trailing-edge Coanda surface is shown to be able to suppress the gust load disturbances. The results show that this control method has a fast frequency response characteristic. More than 50% of the total change in lift coefficient caused by CC can be achieved within the non-dimensional time s=1. This characteristic allows timely adaptive control to counteract the gust disturbances.

The results of unsteady CC verify that by dynamically adapting the momentum coefficients, the gust loads can be eliminated, resulting in a near constant lift under gust condition at subsonic speeds.

Compared to the effectiveness of CC in the subsonic speed range, CC has also shown the capability in alleviating gust load at transonic flows but with a reduced effect due to the 'C_μ-stall' occurring at a much smaller momentum coefficient compared to subsonic range.

Acknowledgments

The authors would like to thank Matthew J. Forster for generously providing the configuration of the 6% thick elliptical circulation control airfoil. The first author would like to acknowledge a studentship from CARDC for him to study for a PhD degree at the University of Sheffield.

References

[1] Guo, S., J. Los, and Y. Liu, Gust Alleviation of a Large Aircraft with a Passive Twist Wingtip. *Aerospace*, 2015. **2**(2): p. 135-154.

[2] Al-Battal, N., D. Cleaver, and I. Gursul, Lift reduction by counter flowing wall jets. *Aerospace Science and Technology*, 2018. **78**: p. 682-695.

[3] Al-Battal, N., D. Cleaver, and I. Gursul, Aerodynamic Load Control through Blowing. *54th AIAA Aerospace Sciences Meeting, AIAA 2016-1820*, 2016.

[4] Alam, M., M. Hromcik, and T. Hanis, Active gust load alleviation system for flexible aircraft: Mixed feedforward/feedback approach. *Aerospace Science and Technology*, 2015. **41**: p. 122-133.

[5] Liu, J., W. Zhang, X. Liu, Q. He, and Y. Qin, Gust response stabilization for rigid aircraft with multi-control-effectors based on a novel integrated control scheme. *Aerospace Science and Technology*, 2018. **79**: p. 625-635.

[6] Fazelzadeh, S.A. and S.M. Jafari, Active control law design for flutter suppression and gust alleviation of a panel with piezoelectric actuators. *Smart Materials & Structures*, 2008. **17**(3).

[7] Liu, X., Q. Sun, and J.E. Cooper, LQG based model predictive control for gust load alleviation. *Aerospace Science and Technology*, 2017. **71**: p. 499-509.

[8] Liu, X. and Q. Sun, Improved LQG Method for Active Gust Load Alleviation. *Journal of Aerospace Engineering*, 2017. **30**(4).

[9] Frost, S., B. Taylor, and M. Bodson, Investigation of Optimal Control Allocation for Gust Load Alleviation in Flight Control. *AIAA Atmospheric Flight Mechanics Conference, AIAA 2012-4858*, 2012.

[10] Hu, J., R. Wang, and D. Huang, Flow control mechanisms of a combined approach using blade slot and vortex generator in compressor cascade. *Aerospace Science and Technology*, 2018. **78**: p. 320-331.

[11] Itsariyapinyo, P. and R.N. Sharma, Large Eddy simulation of a NACA0015 circulation control airfoil using synthetic jets. *Aerospace Science and Technology*, 2018. **82-83**: p. 545-556.

[12] Shmilovich, A. and Y. Yadlin, Flow Control Techniques for Transport Aircraft. *AIAA Journal*, 2011. **49**(3): p. 489-502.

[13] Hammerton, J.R., W. Su, G. Zhu, and S.S.-M. Swei, Optimum distributed wing shaping and control loads for highly flexible aircraft. *Aerospace Science and Technology*, 2018. **79**: p. 255-265.

[14] Yousefi, K., R. Saleh, and P. Zahedi, Numerical study of blowing and suction slot geometry optimization on NACA 0012 airfoil. *Journal of Mechanical Science and Technology*, 2014. **28**(4): p. 1297-1310.

[15] Luedke, J., P. Graziosi, K. Kirtley, and C. Cerretelli, Characterization of Steady Blowing for Flow Control in a Hump Diffuser. *AIAA Journal*, 2005. **43**(8): p. 1644-1652.

[16] Chen, C., R. Seele, and I. Wygnanski, Flow Control on a Thick Airfoil Using Suction Compared to Blowing. *AIAA Journal*, 2013. **51**(6): p. 1462-1472.

[17] Zhang, H., S. Chen, Q. Meng, and S. Wang, Flow separation control using unsteady pulsed suction through endwall bleeding holes in a highly loaded compressor cascade. *Aerospace Science and Technology*, 2018. **72**: p. 455-464.

[18] Greenblatt, D. and I.J. Wygnanski, The control of flow separation by periodic excitation. *Progress in Aerospace Sciences*, 2000. **36**(7): p. 487-545.

[19] Gebhardt, A. and J. Kirz, Numerical investigation of slot variations on the efficiency of tangential blowing at a vertical tailplane with infinite span. *An Official Journal of the Council of European Aerospace Societies*, 2018. **9**(1): p. 195-206.

[20] Xu, X., X. Zhu, Z. Zhou, and R. Fan, Application of Active Flow Control Technique for Gust Load Alleviation. *Chinese Journal of Aeronautics*, 2011. **24**(4): p. 410-416.

[21] de Vries, H., C. Boeije, I. Cleine, E. van Emden, G. Zwart, H. Stobbe, A. Hirschberg, and H. Hoeijmakers, Fluidic Load Control for Wind Turbine Blades. *47th AIAA Aerospace Sciences Meeting including The New Horizons Forum and Aerospace Exposition, AIAA 2009-684*, 2009.

[22] Rao, P., T. Strganac, and O. Rediniotis, Control of aeroelastic response via synthetic jet actuators, in *41st Structures, Structural Dynamics, and Materials Conference and Exhibit*. 2000, American Institute of Aeronautics and Astronautics.

[23] Alexander, M.G., S.G. Anders, S.K. Johnson, J.P. Florance, and D.F. Keller, Trailing Edge Blowing on a Two-Dimensional Six-Percent Thick Elliptical Circulation Control Airfoil Up to Transonic Conditions - NASA/TM-2005-213545. 2005, Sponsoring Organization: NASA Langley Research Center.

[24] Min, B.-Y., W. Lee, R. Englar, and L.N. Sankar, Numerical Investigation of Circulation Control Airfoils. *Journal of Aircraft*, 2009. **46**(4): p. 1403-1410.

[25] Forster, M. and R. Steijl, Design study of Coanda devices for transonic circulation

control. *The Aeronautical Journal*, 2017. **121**(1243): p. 1368-1391.

[26] Cook, M.V., A. Buonanno, and S.D. Erbslöh, A circulation control actuator for flapless flight control. *The Aeronautical Journal*, 2016. **112**(1134): p. 483-489.

[27] Sclafani, A.J., M.A. Dehaan, J.C. Vassberg, C.L. Rumsey, and T.H. Pulliam, Drag Prediction for the Common Research Model Using CFL3D and OVERFLOW. *Journal of Aircraft*, 2014. **51**(4): p. 1101-1117.

[28] Parameswaran, V. and J.D. Baeder, Indicial Aerodynamics in Compressible Flow-Direct Computational Fluid Dynamic Calculations. *Journal of Aircraft*, 1997. **34**(1): p. 131-133.

[29] Singh, R. and J.D. Baeder, Direct Calculation of Three-Dimensional Indicial Lift Response Using Computational Fluid Dynamics. *Journal of Aircraft*, 1997. **34**(4): p. 465-471.

[30] Zhou, Q., G. Chen, A. Da Ronch, and Y. Li, Reduced order unsteady aerodynamic model of a rigid aerofoil in gust encounters. *Aerospace Science and Technology*, 2017. **63**: p. 203-213.

[31] Jones, R.T., The unsteady lift of a wing of finite aspect ratio. 1940, NACA-TR-681.

[32] Wright, J.R., *Introduction to aircraft aeroelasticity and dynamic loads*. Second edition. ed, ed. J.E. Cooper. 2015: Chichester, West Sussex, United Kingdom : Wiley, 2015.

[33] Lomax, H., "Indicial Aerodynamics," AGARD Manual of Aeroelasticity, Part II, Chapter 6. 1960.

[34] Raveh, D.E. and A. Zaide, Numerical Simulation and Reduced-Order Modeling of

Airfoil Gust Response. *AIAA Journal*, 2006. **44**(8): p. 1826-1834.

[35] Theodorsen, T., General Theory of Aerodynamic Instability and the Mechanism of Flutter, NACA-TR-496, Editor. 1949.

[36] Forster, M. and R. Steijl, Numerical Simulation of Transonic Circulation Control. *53rd AIAA Aerospace Sciences Meeting, AIAA 2015-1709*, 2015.

[37] Anders, S.G. and J. Cruz, Assessment of an Unstructured-Grid Method for Predicting Aerodynamic Performance of Jet Flaps. *24th AIAA Applied Aerodynamics Conference, Fluid Dynamics and Co-located Conferences, AIAA 2006-3868*, 2006.

[38] Wetzel, D.A., J. Griffin, and L.N. Cattafesta Iii, Experiments on an elliptic circulation control aerofoil. *Journal of Fluid Mechanics*, 2013. **730**: p. 99-144.

[39] Cruz, J. and S. Anders, Assessment of an Unstructured-Grid Method for Predicting Aerodynamic Performance of Jet Flaps. *24th AIAA Applied Aerodynamics Conference, Fluid Dynamics and Co-located Conferences, AIAA 2006-3868*, 2006.

[40] EUROPEAN AVIATION SAFETY AGENCY - Certification Specifications for Large Aeroplanes CS-25.